

homework III - revise your final project

due 03/01/12, 09:30am, 300-020

Late homework can be dropped off in a box in front of Durand 217. Please mark clearly with date and time @drop off. We will take off 1/10 of points for each 24 hours late, every 12pm after due date. This homework will count 10% towards your final grade.

problem 1 - growth tensors

We have introduced different growth tensors F^g in class. Discuss the following growth tensors.

1.1 $F^g = \vartheta I$

1.2 $F^g = I + [\vartheta - 1] f_0 \otimes f_0$

1.3 $F^g = I + [\vartheta - 1] s_0 \otimes s_0$

1.4 $F^g = \sqrt{\vartheta} I + [1 - \sqrt{\vartheta}] n_0 \otimes n_0$

Here f_0 denotes a distinct fiber direction, s_0 is a sheet direction, n_0 is the normal to a characteristic microstructural plane, and ϑ is a scalar-valued growth multiplier.

For each growth tensor, focus on: (i) its mechanical interpretation, e.g., isotropic, transversely isotropic, orthotropic, generally anisotropic; (ii) its microstructural interpretation, e.g., volumetric growth, fiber lengthening, fiber thickening, area growth; (iii) its biological application, e.g., which type of tissue growth does it characterize, why does this ansatz make sense.

problem 2 - growth tensors

Assume the following microstructural vectors, $f_0 = [1, 0, 0]^t$, $s_0 = [0, 1, 0]^t$, and $n_0 = [0, 0, 1]^t$ aligned with the cartesian coordinates, and a growth multiplier of $\vartheta = 2$.

2.1 Calculate the four growth tensors F^g from 1.1 to 1.4.

2.2 Calculate the volume change of a cube of unit length for all four growth tensors F^g from 1.1 to 1.4 using the Jacobian $J^g = \det(F^g)$.

2.3 Draw a cubic block of tissue of unit length in a three-dimensional coordinate system. Add the unit vectors $dX_1 = [1, 0, 0]^t$, $dX_2 = [0, 1, 0]^t$, and $dX_3 = [0, 0, 1]^t$. For each of the growth tensors F^g in 1.1 to 1.4, calculate and illustrate the deformed vectors dx_1 , dx_2 and dx_3 using $dx = F^g \cdot dX$. Illustrate the grown block.

problem 3 - growing bones in matlab

Last year's class paper "Computational modeling of bone density profiles in response to gait: a subject-specific approach" by Henry Pang, Abhishek Shiwalkar, Chris Mador-mo, and Rebecca Taylor describes bone growth in the tibia. Read the paper carefully.

- 3.1 Download the matlab file package ME337_MATLAB.tar.gz from the coursework website or from our lab website <http://biomechanics.stanford.edu>.
- 3.2 To run the example from the class paper, open the main file `nlin_fem.m` in your matlab editor, and make sure that all input file readings are commented out by a % sign in the first column of lines 6 through 22. The only active input line should be line 10 `ex_henry`.
- 3.3 In the command window, call the main file by typing `nlin_fem` and wait for the mesh to be generated.
- 3.4 Run the density evolution algorithm for 5 time steps by typing `step,,5`. Describe what you see in the command window and in the graphics window. How many iterations does a typical load step take to find the equilibrium of the nonlinear problem? Focus on load step 5. Report the residuals, i.e., the errors in solution, to demonstrate quadratic convergence of the Newton Raphson scheme.
- 3.5 Then, run the algorithm for an additional 35 time steps by typing `step,,35` in the command window. Quit the algorithmic environment by typing `quit`. There are two major fields that describe the geometry of a finite element input file, in this case Henry's tibia. Type `q0` to show one of them and then `size(q0)`. What does the `q0` field contain? Type `edof` to show one of them and then `size(edof)`. What does the `edof` field contain?
- 3.6 Learn to fake your results! Most people show finite element results in terms of colorful plots. Here, the color figures are produced in the subroutine `plot_int.m`. You can easily manipulate a plot by changing the color axis. Type `caxis([0.5 1.5])` to change the color axis and observe what happens. Type `caxis([0.00 1.25])` to change the color axis back again. You can then plot your final figure, e.g., by `print('-depsc','-r300','figure01.eps')`.
- 3.7 You have now entirely reproduced Henry's bone density profile. Compare your `figure01.eps` with Figure 6 in last year's class paper. What is different? Do you have an idea why?
- 3.8 Now, pretend Henry's gait analysis had resulted in a different input for the finite element simulation. Open the input file `ex_henry.m`. In lines 64 through 67, you can see how the load is generated. Keep the medial load as it is, but assume that the lateral load was not applied at node 248 but at node 123. Modify your input file accordingly, save it, and rerun the simulation `nlin_fem` for `step,,40` time steps.

Quit your algorithmic environment by typing quit. Plot your final figure with `print('-depsc', '-r300', 'figure02.eps')`.

- 3.8 Compare both figures, `figure01.eps` and `figure02.eps`, in three to five sentences and attach them to your homework.

For this part of the homework, it is okay to work in groups, especially if you are not very familiar with matlab. If you create the results in a group, however, the results, interpretations, and discussions must be written individually by each group member. Each group member must understand the matlab algorithm.

problem 4 - wikipedia websites on growth

Create or edit a wikipedia website on growth. To create a site, you can think of any growth example. To edit a site, e.g., go to http://en.wikipedia.org/wiki/Wolff's_law or http://en.wikipedia.org/wiki/Tissue_expansion. Add at least one paragraph of text with at least two references. Ideally, even add a figure. Print your submission and hand it in with your homework.

problem 5 - revise your final project

- 5.1 Download the style file `me337_project_sample.doc` from the coursework website and paste in your title, outline, opening sentence, introduction, schematic drawing, and references from homework II.
- 5.2 Expand the reference section to at least three key references and seven additional references. Make sure your citations all have the same style. I will take off points if they don't! This is what some picky reviewers criticize first before even reading your paper.
- 5.3 Revise your introduction and make sure that all your references are cited. The introduction should: (i) contain your catchy opening sentence with citation, (ii) motivate your work, and (iii) give an overview of the current state of the field. It should be one to two columns long.
- 5.4 Draft an outline of all the figures you would like to include in your manuscript. This is the most important step of drafting your paper, since most scientific papers are written around figures. For each figure, create a place holder or the figure itself. Create meaningful figure captions. The figure captions in the sample file are actually not a good example. In the biological literature, captions are usually more detailed and can be several lines long. When you adopt figures from the literature, cite your source. Remember that in a real journal paper, you cannot use other authors' figures without copyright agreement.

Computational modeling of bone density profiles in response to gait: a subject-specific approach

Henry Pang · Abhishek P. Shiwalkar ·
Chris M. Madormo · Rebecca E. Taylor ·
Thomas P. Andriacchi · Ellen Kuhl

Received: 2 February 2011 / Accepted: 8 May 2011 / Published online: 22 May 2011
© Springer-Verlag 2011

Abstract The goal of this study is to explore the potential of computational growth models to predict bone density profiles in the proximal tibia in response to gait-induced loading. From a modeling point of view, we design a finite element-based computational algorithm using the theory of open system thermodynamics. In this algorithm, the biological problem, the balance of mass, is solved locally on the integration point level, while the mechanical problem, the balance of linear momentum, is solved globally on the node point level. Specifically, the local bone mineral density is treated as an internal variable, which is allowed to change in response to mechanical loading. From an experimental point of view, we perform a subject-specific gait analysis to identify the relevant forces during walking using an inverse dynamics approach. These forces are directly applied as loads in the finite element simulation. To validate the model, we take a Dual-Energy X-ray Absorptiometry scan of the subject's right knee from which we create a geometric model of the proximal tibia. For qualitative validation, we compare the computationally predicted density profiles to the bone

mineral density extracted from this scan. For quantitative validation, we adopt the region of interest method and determine the density values at fourteen discrete locations using standard and custom-designed image analysis tools. Qualitatively, our two- and three-dimensional density predictions are in excellent agreement with the experimental measurements. Quantitatively, errors are less than 3% for the two-dimensional analysis and less than 10% for the three-dimensional analysis. The proposed approach has the potential to ultimately improve the long-term success of possible treatment options for chronic diseases such as osteoarthritis on a patient-specific basis by accurately addressing the complex interactions between ambulatory loads and tissue changes.

Keywords Growth · Open system thermodynamics · Density · Bone · Finite elements · Gait analysis

1 Motivation

Osteoarthritis is the most prevalent joint disorder in the world and remains one of the few chronic diseases of aging for which there is little to no effective treatment (Hunter and Felson 2006). It is the leading cause of chronic disability in the United States affecting almost 27 million Americans (Altman 2010). Shedding light on the causes and progression of osteoarthritis has the potential to drastically improve the quality of life for the millions of sufferers. Although osteoarthritis in articular tissues is widely believed to be a disease of the cartilage alone, some studies indicate that changes in subchondral bone density are associated with cartilage damage in the knee (Hunter and Felson 2006; Radin and Rose 1986). In particular, it has been shown that an increase in subchondral density leads to a loss of the shock absorbing capacity of the bone, causing increased transmission of loads into the

H. Pang · A. P. Shiwalkar · C. M. Madormo · R. E. Taylor ·
T. P. Andriacchi · E. Kuhl (✉)
Department of Mechanical Engineering, Stanford University,
Stanford, CA 94305, USA
e-mail: ekuhl@stanford.edu

T. P. Andriacchi
Department of Orthopaedics, Stanford University,
Stanford, CA 94305, USA

E. Kuhl
Department of Bioengineering, Stanford University,
Stanford, CA 94305, USA

E. Kuhl
Department of Cardiothoracic Surgery, Stanford University,
Stanford, CA 94305, USA

cartilage (Dequeker et al. 1997). This argument identifies the subchondral bone, the region just below the cartilage, as an important area of interest in current osteoarthritis research.

Osteoarthritis is a multifactorial process in which mechanical factors play a key role (Andriacchi 1994). It is characterized through changes in structure and function of the entire joint, including the subchondral bone, menisci, ligaments, periarticular muscle, capsule, and synovium. Knee osteoarthritis typically affects the tibiofemoral compartment on the medial side of the knee (Hulet et al. 2002). This is most likely due to the fact that a majority of the load generated during walking is transmitted through this side (Baliunas et al. 2002). As a result, the bone mineral content is typically significantly larger in the medial than in the lateral plateau (Hurwitz et al. 1998). Thorough clinical studies have investigated the asymmetric load division between the medial and lateral compartments during normal walking (Schipplein and Andriacchi 1991). The first mathematical model that studied force transmission through the knee joint at the medial and lateral condyles using force plate analyses dates back to the early 70s (Morrison 1970). While a significant amount of research has been dedicated to the role of the subchondral bone in the development of osteoarthritis within the past four decades, there is a knowledge gap in terms of integrating all these findings into a single unique tool to reliably predict global density profiles on a patient-specific basis.

In the mid 70s, first mechanistic models were proposed to characterize the functional adaptation of bone in response to loading (Ambrosi et al. 2011; Cowin and Hegedus 1976). Conceptually speaking, these approaches model bone within the framework of open system thermodynamics (Kuhl and Steinmann 2003b; Menzel 2005), allowing it to adapt its density in response to changes in the mechanical environment (Himpel et al. 2005; Kuhl and Steinmann 2003c). Within the past two decades, finite element models have been recognized as a powerful tool to investigate bone and tissue growth (Huiskes et al. 1987; Jacobs et al. 1995). Finite element simulations can be used to predict bone growth and resorption in response to various different loading patterns that would not be feasible to study experimentally (Reina-Romo et al. 2010; Weinans et al. 1992). They also allow for efficient parameter studies, which can be used to identify key contributors to bone growth (Carpenter and Carter 2010a; Hambli et al. 2011), bone straightening (Carpenter and Carter 2010b), bone torsion (Taylor et al. 2008), or bone failure (Gitman et al. 2010; Zhang et al. 2010). Although promising, the use of finite element models to predict bone mineral density in osteoarthritis is still in its developmental stages, and the validation of the underlying models remains largely qualitative.

The goal of this study is therefore to qualitatively and quantitatively explicate how forces during gait affect the bone density distribution in the proximal tibia using a combined experimental-computational approach. In a

multi-faceted series of studies including gait analysis, Dual-Energy X-ray Absorptiometry, bone mineral density analysis, and two- and three-dimensional finite element analyses, we integrate data from multiple sources to explore the interplay between biological and mechanical equilibrium. To prototype this approach for a representative subject, we first perform a gait analysis. Using an inverse dynamics approach, we reconstruct force vectors with a precise information of magnitude, location, and direction of the forces experienced by the tibia during gait. We apply these load vectors directly to a finite element analysis that allows us to predict a subject-specific bone density profile. The underlying geometric model is extracted from a Dual-Energy X-ray Absorptiometry scan of the subject's right knee. This scan also serves to validate the computational density prediction. For qualitative validation, we compare characteristic features of the density profiles from experiment and simulation. For quantitative validation, we adopt the region of interest method and extract discrete density values using image analysis tools.

This manuscript is organized as follows. In Sect. 2, we briefly summarize the continuum approach toward density growth in terms of kinematic equations, balance equations, and constitutive equations. Next, in Sect. 3, we discuss their computational solution with a particular focus on the local and global Newton iterations for biological and mechanical equilibrium. The design of a subject-specific geometric model based on Dual-Energy X-ray Absorptiometry is illustrated in Sect. 4. We then demonstrate the measurement of the tibial joint forces through a gait analysis in Sect. 5. In Sect. 6, we integrate all these pieces of information in a subject-specific two- and three-dimensional finite element-based density prediction. We conclude with an error analysis by comparing computationally predicted and experimentally measured bone mineral density profiles. Last, in Sect. 7, we discuss the overall results and illustrate the clinical potential of the proposed approach.

2 Continuum modeling of density growth

In this section, we illustrate the governing equations of density growth within the framework of open system thermodynamics (Kuhl and Steinmann 2003b, 2004). We briefly summarize the kinematic equations, the balance equations, and the constitutive equations.

2.1 Kinematics

We adopt the kinematics of finite deformations and introduce the deformation map φ , which, at any given time t , maps the material placement X of a physical particle in the material configuration \mathcal{B}_0 to its spatial placement \mathbf{x} in the spatial

configuration \mathcal{B}_t .

$$\mathbf{x} = \boldsymbol{\varphi}(\mathbf{X}, t) \quad (1)$$

In the following, we apply a formulation which is entirely related to the material frame of reference. Accordingly, $\nabla\{\bullet\} = \partial_X\{\bullet\}|_t$ and $\text{Div}\{\bullet\} = \partial_X\{\bullet\}|_t : \mathbf{I}$ denote the gradient and the divergence of any field $\{\bullet\}(\mathbf{X}, t)$ with respect to the material placement \mathbf{X} at fixed time t , where \mathbf{I} is the material identity tensor. In this notation, the deformation gradient \mathbf{F} , which defines the linear tangent map from the material tangent space $T\mathcal{B}_0$ to the spatial tangent space $T\mathcal{B}_t$, takes the following representation.

$$\mathbf{F} = \nabla\boldsymbol{\varphi}(\mathbf{X}, t) \quad (2)$$

Its determinant introduces the Jacobian $J = \det \mathbf{F} > 0$, which characterizes volumetric changes. In what follows, $\{\dot{\bullet}\} = \partial_t\{\bullet\}|_X$ denotes the material time derivative of any field $\{\bullet\}(\mathbf{X}, t)$ at fixed material placement \mathbf{X} . We would like to point out that, for the sake of completeness, we have chosen a general nonlinear kinematic formulation here, although bone, in the physiological range, only experiences infinitesimal strains. However, this generalization does not induce any additional complexities, since the overall set of equations turns out to be nonlinear, and will, therefore, have to be solved using a nonlinear solution scheme anyways.

2.2 Balance equations of open systems

In open system thermodynamics, the balance of mass balances the rate of change of the material density $\dot{\rho}_0$ with a possible in- or outflux of mass \mathbf{R} and mass source \mathcal{R}_0 .

$$\dot{\rho}_0 = \text{Div} \mathbf{R} + \mathcal{R}_0 \quad (3)$$

Similarly, the balance of linear momentum balances the density-weighted rate of change of the momentum $\dot{\mathbf{v}}$, where $\mathbf{v} = \dot{\boldsymbol{\varphi}}$ is nothing but the spatial velocity, with the momentum flux \mathbf{P} and the momentum source \mathbf{b}_0 .

$$\rho_0 \dot{\mathbf{v}} = \text{Div} \mathbf{P} + \mathbf{b}_0 \quad (4)$$

The above equation represents the mass-specific version of the balance of momentum, which is particularly useful in the context of growth, since it contains no explicit dependencies on the changes in mass (Kuhl and Steinmann 2003a,b).

2.3 Constitutive equations of density growth

Last, we specify constitutive equations for the mass flux \mathbf{R} , the mass source \mathcal{R}_0 , the momentum flux \mathbf{P} , and the momentum source \mathbf{b}_0 . The mass flux \mathbf{R} is typically related to an interstitial fluid flow and to concentration gradients in the individual bone constituents (Ambrosi et al. 2011). To avoid the use of sophisticated mixture theories (Reina-Romo et al.

2010), here, we assume that the mass flux is negligibly small,

$$\mathbf{R} = \mathbf{0} \quad (5)$$

and that all changes in mass can be attributed exclusively to the mass source \mathcal{R}_0 . Accordingly, we propose an energy-based format for the mass source,

$$\mathcal{R}_0 = c \left[[\rho_0 / \rho_0^*]^{-m} \psi_0 - \psi_0^* \right] \quad (6)$$

where ψ_0 is the free energy, ρ_0^* is the initial density, ψ_0^* is the target energy or stimulus, and m is a unit-less algorithmic exponent that ensures the stability of the adaptation algorithm (Harrigan and Hamilton 1993). The parameter c is of the unit time divided by length squared and governs the speed of the adaption process. In the context of porous materials, the free energy

$$\psi_0 = [\rho_0 / \rho_0^*]^n \psi_0^{\text{neo}} \quad (7)$$

is typically characterized through the elastic free energy, e.g., of Neo-Hookean type,

$$\psi_0^{\text{neo}} = \frac{1}{2} [\lambda \ln^2(J) + \mu [\mathbf{F} \cdot \mathbf{F} - 3 - 2 \ln(J)]] \quad (8)$$

scaled by the relative density $[\rho_0 / \rho_0^*]^n$. Here, λ and μ are the classical Lamé parameters. The unit-less porosity exponent n typically varies between $1 \leq n \leq 3.5$ depending on the particular open-pored ground substance (Carter and Hayes 1977). This particular choice of the free energy defines the Piola stress

$$\mathbf{P} = \frac{\partial \psi_0}{\partial \mathbf{F}} = [\rho_0 / \rho_0^*]^n \mathbf{P}^{\text{neo}} \quad (9)$$

as the classical Neo-Hookean stress

$$\mathbf{P}^{\text{neo}} = \frac{\partial \psi_0^{\text{neo}}}{\partial \mathbf{F}} = \mu \mathbf{F} + [\lambda \ln(J) - \mu] \mathbf{F}^{-t} \quad (10)$$

weighted by the relative density $[\rho_0 / \rho_0^*]^n$. For the sake of simplicity, we assume that the momentum source

$$\mathbf{b}_0 = \mathbf{0} \quad (11)$$

vanishes identically. The momentum source could be critical, for example, to characterize density adaptation in a low gravity environment, e.g., loss of bone in space.

3 Computational modeling of density growth

In this section, we briefly reiterate the computational model for density growth within the framework of a nonlinear finite element analysis. To simplify the model, we apply four common assumptions. For the biological equilibrium Eq. (3), we assume that the mass flux is significantly smaller than the mass source and therefore negligible, i.e., $\mathbf{R} = \mathbf{0}$. This implies that we can apply a C^{-1} -continuous interpolation of the density ρ_0 , which suggests that it can be treated locally as

an internal variable on the integration point level (Kuhl et al. 2003; Kuhl and Steinmann 2003a). For the mechanical equilibrium Eq. (4), we assume that gravity effects are negligible, i.e., $\mathbf{b}_0 = \mathbf{0}$, that no traction is acting on the bone surface, i.e., $\mathbf{P} \cdot \mathbf{N} = \mathbf{0}$, and that the time scale of the biological problem is much larger than the time scale of the mechanical problem, i.e., $\dot{\mathbf{v}} = \mathbf{0}$. This implies that we can neglect volume forces, apply homogeneous Neumann boundary conditions, and treat the mechanical problem as quasi static.

3.1 Local Newton iteration—biological equilibrium

With the simplifying assumption of a vanishing mass flux, $\mathbf{R} = \mathbf{0}$, the biological equilibrium Eq. (3) remains strictly local, and we can solve it locally on the integration point level. To discretize it in time, we partition the time interval of interest \mathcal{T} into n_{stp} subintervals,

$$\mathcal{T} = \bigcup_{k=1}^{n_{\text{stp}}} [t^k, t^{k+1}] \quad (12)$$

and focus on the interval $[t^k, t^{k+1}]$ for which $\Delta t = t^{k+1} - t^k > 0$ denotes the current time increment. Our goal is to determine the reference density ρ_0 for a given deformation state $\boldsymbol{\varphi}$ at time t^{k+1} and a given reference density ρ_0^k at the end of the previous time step t^k . Note that for the sake of compactness, we have omitted the index $k+1$ for all quantities at the end of the current time step t^{k+1} . To approximate the material time derivative $\dot{\rho}_0$, we introduce the following finite difference approximation.

$$\dot{\rho}_0 = [\rho_0 - \rho_0^k] / \Delta t \quad (13)$$

In the spirit of implicit time stepping schemes, we now reformulate the balance of mass (3) with the help of this finite difference approximation, introducing the discrete residual \mathbf{R}^ρ in terms of the unknown reference density ρ_0 .

$$\mathbf{R}^\rho = \rho_0 - \rho_0^k - c \left[[\rho_0 / \rho_0^*]^{[n-m]} \psi_0^{\text{neo}} - \psi_0^* \right] \Delta t \doteq 0 \quad (14)$$

We suggest to solve this nonlinear residual equation for the unknown reference density using a local Newton iteration. Within each iteration step, we calculate the linearization of the residual \mathbf{R}^ρ with respect to the reference density ρ_0 ,

$$\mathbf{K}^\rho = \frac{d\mathbf{R}^\rho}{d\rho_0} = 1 - c [n-m] \frac{1}{\rho_0} [\rho_0 / \rho_0^*]^{[n-m]} \psi_0^{\text{neo}} \Delta t \quad (15)$$

to determine the iterative update of the unknown reference density $\rho_0 \leftarrow \rho_0 - \mathbf{R}^\rho / \mathbf{K}^\rho$ until convergence is achieved, i.e., until the update $\Delta\rho_0 = -\mathbf{R}^\rho / \mathbf{K}^\rho$ is below a user-defined threshold value.

3.2 Global Newton iteration—mechanical equilibrium

With the simplifying assumptions of a vanishing momentum source, $\mathbf{b}_0 = \mathbf{0}$, and negligible inertia effects, $\dot{\mathbf{v}} = \mathbf{0}$, the mechanical equilibrium Eq. (4) reduces to the internal force balance, $\text{Div } \mathbf{P} = \mathbf{0}$. We cast it into its weak form, $\mathbf{G}^\varphi = \int_{\mathcal{B}_0} \nabla \delta \boldsymbol{\varphi} : \mathbf{P} \, dV \doteq 0$, through the multiplication with the test function $\delta \boldsymbol{\varphi}$ and the integration over the domain of interest \mathcal{B}_0 to solve it globally on the node point level. To discretize it in space, we partition the domain of interest \mathcal{B}_0 into n_{el} finite elements \mathcal{B}_0^e .

$$\mathcal{B}_0 = \bigcup_{e=1}^{n_{\text{el}}} \mathcal{B}_0^e \quad (16)$$

Our goal is to determine the deformation state $\boldsymbol{\varphi}$ for a given loading at time t . To approximate the test function $\delta \boldsymbol{\varphi}$, the unknown deformation $\boldsymbol{\varphi}$, and their gradients $\nabla \delta \boldsymbol{\varphi}$ and $\nabla \boldsymbol{\varphi}$, we apply an isoparametric Bubnov-Galerkin based finite element interpolation,

$$\begin{aligned} \delta \boldsymbol{\varphi} &= \sum_{i=1}^{n_{\text{en}}} N^i \delta \boldsymbol{\varphi}_i, & \nabla \delta \boldsymbol{\varphi} &= \sum_{i=1}^{n_{\text{en}}} \delta \boldsymbol{\varphi}_i \otimes \nabla N^i \\ \boldsymbol{\varphi} &= \sum_{j=1}^{n_{\text{en}}} N^j \boldsymbol{\varphi}_j, & \nabla \boldsymbol{\varphi} &= \sum_{j=1}^{n_{\text{en}}} \boldsymbol{\varphi}_j \otimes \nabla N^j \end{aligned} \quad (17)$$

where N are the element shape functions, and $i, j = 1, \dots, n_{\text{en}}$ are the element nodes. We now reformulate the weak form of the balance of linear momentum (4) with the help of these finite element approximations, introducing the discrete residual \mathbf{R}_I^φ in terms of the unknown nodal deformation $\boldsymbol{\varphi}_J$.

$$\mathbf{R}_I^\varphi = \mathbf{A} \int_{\mathcal{B}_e} \nabla N_\varphi^i \cdot \mathbf{P} \, dV_e \doteq \mathbf{0} \quad (18)$$

Herein, the operator \mathbf{A} symbolizes the assembly of all element residuals at the $j = 1, \dots, n_{\text{en}}$ element nodes to the overall residual at the global node points $J = 1, \dots, n_{\text{el}}$. Again, we suggest an incremental iterative Newton algorithm to solve the nonlinear residual equation for the unknown deformation. The consistent linearization of the residual \mathbf{R}_I^φ with respect to the nodal vector of unknowns $\boldsymbol{\varphi}_J$ introduces the global stiffness matrix.

$$\mathbf{K}_{IJ}^\varphi = \frac{\partial \mathbf{R}_I^\varphi}{\partial \boldsymbol{\varphi}_J} = \mathbf{A} \int_{\mathcal{B}_e} \nabla N_\varphi^i \cdot \mathbf{A} \cdot \nabla N_\varphi^j \, dV_e \quad (19)$$

Upon convergence of the local Newton iteration described in the Sect. 3.1, we calculate the Piola stress

$$\mathbf{P} = [\rho_0 / \rho_0^*]^n [\mu \mathbf{F} + [\lambda \ln(J) - \mu] \mathbf{F}^{-t}] \quad (20)$$

locally at the integration point level to evaluate the global residual (18). Last, to evaluate the global stiffness matrix

Table 1 Computational modeling of density growth embedded in non-linear finite element algorithm

global Newton iteration
loop over all elements
loop over all integration points
compute elastic stress & tangent $\mathbf{P}^{\text{neo}}, \mathbf{A}^{\text{neo}}$ (10,22)
local Newton iteration
compute residual & linearization $\mathbf{R}^\rho, \mathbf{K}^\rho$ (14,15)
update density $\rho_0 \leftarrow \rho_0 - \mathbf{K}^{\rho-1} \mathbf{R}^\rho$
compute growth stress & tangent \mathbf{P}, \mathbf{A} (9,21)
compute residual & linearization $\mathbf{R}_I^\varphi, \mathbf{K}_{IJ}^\varphi$ (18,19)
update deformation $\varphi_J \leftarrow \varphi_J - \mathbf{K}_{IJ}^{\varphi-1} \cdot \mathbf{R}_I^\varphi$

The balance of mass is evaluated locally with the density stored at the integration point level, while the balance of linear momentum is evaluated globally with the deformation stored at the node point level

(19), we linearize the algorithmic Piola stress to obtain the algorithmic constitutive moduli,

$$\mathbf{A} = \frac{d\mathbf{P}}{d\mathbf{F}} = \frac{\partial \mathbf{P}}{\partial \mathbf{F}} \bigg|_{\rho_0} + \frac{\partial \mathbf{P}}{\partial \rho_0} \bigg|_{\mathbf{F}} \otimes \frac{\partial \rho_0}{\partial \mathbf{R}_0} \frac{\partial \mathbf{R}_0}{\partial \mathbf{F}} = [\rho_0 / \rho_0^*]^n \mathbf{A}^{\text{neo}} + \gamma \mathbf{P} \otimes \mathbf{P} \quad (21)$$

which we evaluate locally on the integration point level. The first term is nothing but the density-scaled tangent operator of the classical Neo-Hookean material,

$$\mathbf{A}^{\text{neo}} = \frac{d\mathbf{P}^{\text{neo}}}{d\mathbf{F}} = \lambda \mathbf{F}^{-t} \otimes \mathbf{F}^{-t} + [\mu - \lambda \ln(J)] \mathbf{F}^{-t} \otimes \mathbf{F}^{-t} + \mu \mathbf{I} \otimes \mathbf{I} \quad (22)$$

where we have used the following abbreviations, $\{\bullet \otimes \circ\}_{ijkl} = \{\bullet\}_{ik} \{\circ\}_{jl}$ and $\{\bullet \otimes \circ\}_{ijkl} = \{\bullet\}_{il} \{\circ\}_{jk}$, for its nonstandard fourth order products. Finally, the scalar coefficient γ takes the following format.

$$\gamma = \frac{c n [\rho_0 / \rho_0^*]^{-m} \Delta t}{\rho_0 - c [n - m] [\rho_0 / \rho_0^*]^{[n-m]} \psi_0^{\text{neo}} \Delta t} \quad (23)$$

For each global Newton iteration step, we iteratively update the current deformation state $\varphi \leftarrow \varphi - \mathbf{K}_{IJ}^{\varphi-1} \cdot \mathbf{R}_I^\varphi$ until we achieve algorithmic convergence. Upon convergence, we store the corresponding reference density ρ_0 at the integration point level. The finite element algorithm for density growth is implemented in Matlab and summarized in Table 1, see also Kuhl et al. (2003); Taylor et al. (2008).

4 Subject-specific geometry and density profile

In this section, we briefly summarize the generation of the Dual-Energy X-ray Absorptiometry scan of the subject's tibiofemoral joint which serves dual purpose. Using this scan, we create a subject-specific geometric model of the proximal tibia and characterize the subject-specific density profile for later model validation.

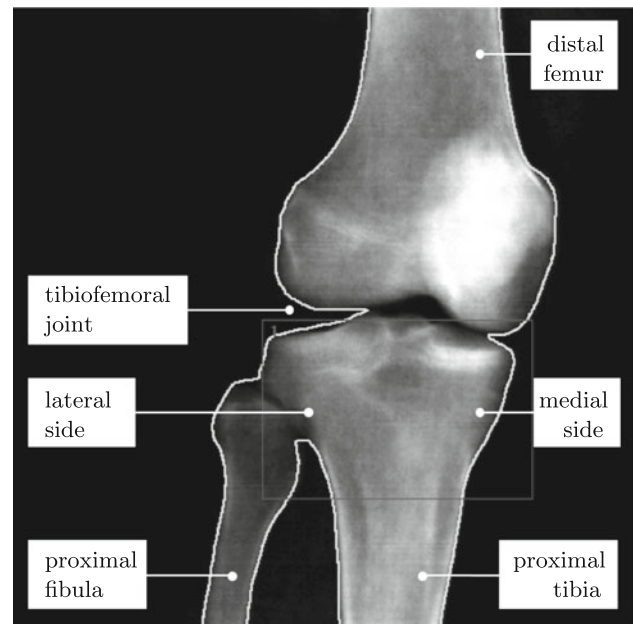


Fig. 1 Characterization of density profile through Dual-Energy X-ray Absorptiometry, DEXA, of the study subject's right knee. A subject-specific geometric model of the proximal tibia is generated from the outline of the DEXA scan. The gray-scale coded bone mineral density measurement is used to validate our bone growth model

4.1 Bone mineral density

Dual-Energy X-ray Absorptiometry, or DEXA scanning, is currently the most common technique to measure bone mineral density (Bolotin 2007). It is based on two X-ray beams with different energy levels, which are directed at the bone.

The degree by which these beams are absorbed by the bone is an integral measure of the bone mineralization along the beam axis, which can be converted into the bone mineral density (Nielsen 2000). Although recent studies have demonstrated that bone mineral density measured via DEXA lacks both sensitivity and selectivity to effectively identify patients with decreased bone strength and at risk of fracture (Bone et al. 2005; Kaptoge et al. 2005), the DEXA scan remains the current clinical standard to diagnose bone loss and osteoporosis (Gandolini and Salvioni 2004). Here, to generate a subject-specific geometry of the proximal tibia and to validate our bone growth model, we take a DEXA scan of our study subject's right knee. This scan of the tibiofemoral joint provides quantitative information about the bone mineral density in the distal femur, the proximal fibula, and the proximal tibia, see Fig. 1.

4.2 Two-dimensional tibia model

To create a two-dimensional geometric model of the subject's right proximal tibia, we outline the tibial surface from the DEXA scan, see Fig. 1. The outline is imported into Matlab

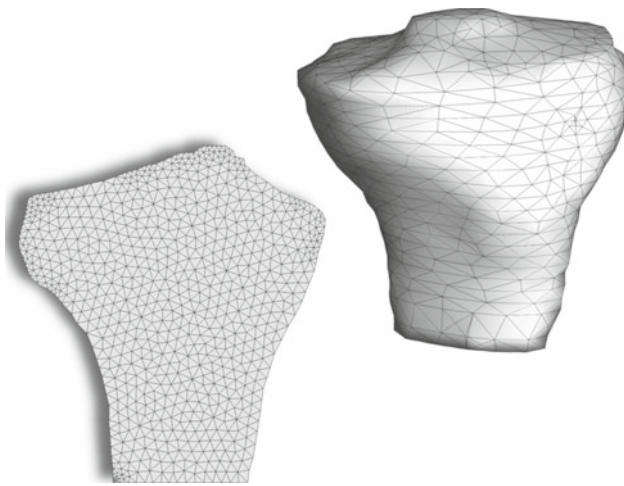


Fig. 2 Finite element meshes of the proximal tibia. The subject-specific two-dimensional mesh consists of 1,416 linear triangular elements, 782 nodes, and 1,564 degrees of freedom, *left*. The generic three-dimensional mesh consists of 3,190 linear tetrahedral elements, 893 nodes, and 2,679 degrees of freedom, *right*

and then meshed with two-dimensional triangular elements. The resulting mesh consists of 1,416 linear triangular elements connected at 782 nodes and has 1,564 degrees of freedom, see Fig. 2, left.

4.3 Three-dimensional tibia model

To generate a generic three-dimensional geometric model, we discretize the magnetic resonance image of a randomly selected healthy adult right knee from our database. We create a three-dimensional mesh, which contains 3,190 linear tetrahedral elements connected at 893 nodes, introducing 2,679 degrees of freedom, see Fig. 2, right.

5 Subject-specific forces during gait

We determine the maximum forces acting on the tibia during walking through a gait analysis (Andriacchi et al. 2004). In gait analysis experiments, force platforms are used to measure ground reaction forces acting on the body, while video-based motion capture techniques are applied to record the three-dimensional positions and orientations of characteristic body segments. To identify these segments, passive markers that reflect infrared radiation are placed strategically on anatomic landmarks of the subject's lower right extremity including the right hip joint, the knee joint, and the ankle joint, see Fig. 3.

The subject performs three walking trials at a self-selected normal speed. An eight-camera opto-electronic system for three-dimensional motion analysis is used to record lower limb kinematics. Ground reaction forces are collected using a multi-component force plate placed in the center of the walk-

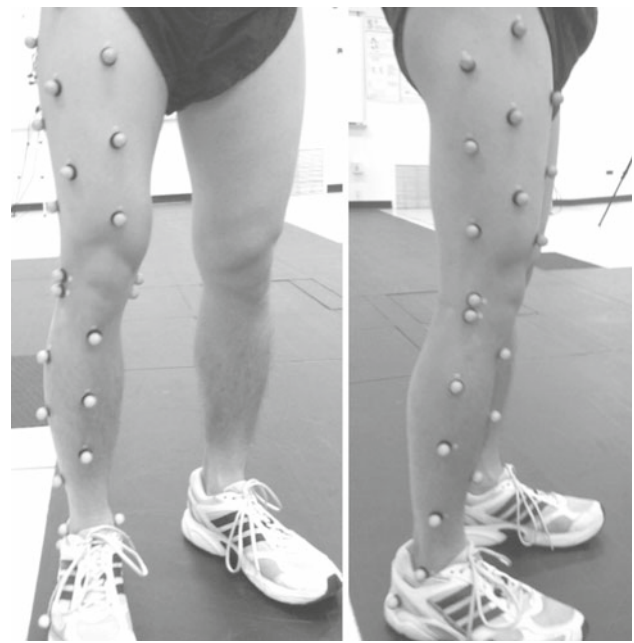


Fig. 3 Characterization of peak loads through gait analysis. Reflective markers are placed on the subject's lower *right* extremity. Maximum knee forces are calculated from measured marker kinematics and force plate data using an inverse dynamics approach, Andriacchi et al. (1997)

Table 2 Maximum forces in the knee averaged over three gait cycles

Trial	I	II	III	Mean
Max knee force [N]	552	549	579	560
Max knee force [% BW]	94.9	94.4	99.4	96.2

Inverse dynamics are used to determine the knee reaction forces from the measured ground reaction force

way. Marker kinematics and force plate data are sampled at a frequency of 120 Hz. In a postprocessing analysis, joint forces and adduction moments in the hip, knee, and ankle joint are calculated from marker kinematics and force data using an inverse dynamics approach (Andriacchi et al. 1997). We choose the maximum ground reaction force during the midstance phase of gait as the relevant load case. The resulting maximum knee forces of all three walking trial are summarized in Table 2. We identify an average maximum knee force of 560 N. To account for asymmetric loading between the medial and lateral compartments, we apply 45% of the total gait load to the lateral side and 55% to the medial side Zhao et al. (2007), resulting in lateral and medial forces of 252 N and 308 N, respectively, see Fig. 4.

6 Subject-specific density prediction

To predict the bone in the right proximal tibia, we perform two- and three-dimensional nonlinear finite element analyses

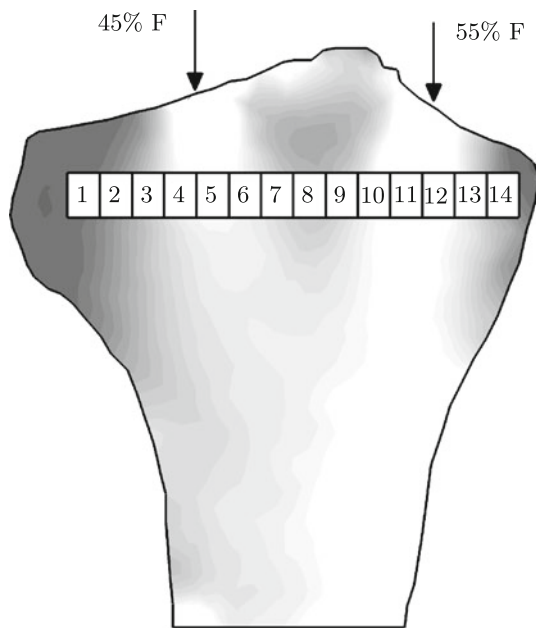


Fig. 4 Region of interest method to characterize regional density variations in the proximal tibia. The local bone mineral density, BMD, is evaluated in fourteen equal-sized regions along the tibial width, [Hulet et al. \(2002\)](#). Bone mineral densities of the lateral and medial tibial plateau are identified as regional averages over three neighboring regions, $BMD_{lat} = [BMD_2 + BMD_3 + BMD_4]/3$ and $BMD_{med} = [BMD_{11} + BMD_{12} + BMD_{13}]/3$. To account for asymmetric loading between the medial and lateral compartments, we apply 45% of the total gait load to the lateral side and 55% to the medial side, [Zhao et al. \(2007\)](#)

based on a Matlab implementation of the algorithm described in Sect. 3. We use the finite element discretizations illustrated in Fig. 2, which consist of 1,416 linear triangular elements, 782 nodes, and 1,564 degrees of freedom for the two-dimensional model, and of 3,190 linear tetrahedral elements, 893 nodes, and 2,679 degrees of freedom for the three-dimensional model. For the elastic material model, we choose the Lamé parameters to $\lambda = 2,186 \text{ N/mm}^2$ and $\mu = 1,458 \text{ N/mm}^2$, corresponding to a Young's modulus of $E = 3,790 \text{ N/mm}^2$ and a Poisson's ratio of $\nu = 0.3$, see [Carter and Hayes \(1977\)](#); [Lancianese et al. \(2008\)](#). For the growth model, we choose the initial density to $\rho_0^* = 1.0 \text{ g/cm}^3$, the target energy to $\psi_0^* = 0.00275 \text{ N/mm}^2$, the porosity exponent to $n = 2.0$, and the algorithmic exponent to $m = 3$, see [Harrigan and Hamilton \(1993\)](#), [Kuhl et al. \(2003\)](#).

Using the knee forces identified through the gait analysis in Sect. 5, we apply the average vertical force of three walking trials during the midstance phase of gait, 560 N. Figure 4 illustrates the resulting knee forces with 45% of the total force, 252 N, applied to the lateral side and 55%, 308 N, applied to the medial side ([Zhao et al. 2007](#)). As indicated in Sect. 3, we neglect the body forces of the tibia and assume that shear forces acting on the tibia are negligible because of the aligning action of the articular cartilage in

contact with the subchondral bone. We apply zero Dirichlet boundary conditions to the nodes at the distal end of the tibia.

To quantify regional density variations and to validate our model, we adopt the region of interest method ([Hulet et al. 2002](#)) and evaluate the local bone mineral density, BMD, in fourteen equal-sized regions along the tibial width, see Fig. 4. The subject-specific local bone mineral density in these fourteen regions is automatically extracted from the DEXA scan. The computationally predicted density is computed from gray-scaled bone density profiles by averaging the density values of the approximately 1,000 pixels within each region using Matlab. The bone mineral densities of the lateral and medial tibial plateaus are identified as regional averages over three neighboring regions, $BMD_{lat} = [BMD_2 + BMD_3 + BMD_4]/3$ and $BMD_{med} = [BMD_{11} + BMD_{12} + BMD_{13}]/3$, see [Hulet et al. \(2002\)](#).

6.1 Two-dimensional density prediction

To demonstrate the convergence of the algorithm, we first explore the evolution of the mass source \mathcal{R}_0 , which is the driving force for density changes, see Fig. 5. Since we start with an initially homogeneous density distribution, we observe the largest deposition of bone underneath the loaded areas, shown in red, while unloaded areas undergo bone resorption, shown in blue. As time progresses, from left to right, the bone density changes such that the strain energy $[\rho_0/\rho_0^*]^{n-m} \psi_0$ converges toward the biological stimulus ψ_0^* . At biological equilibrium, right, strain energy and biological stimulus are identical, $[\rho_0/\rho_0^*]^{n-m} \psi_0 = \psi_0^*$, the density source \mathcal{R}_0 vanishes and the density ρ_0 undergoes no further changes.

The heterogeneous mass source generates a heterogeneous density profile which is shown in Fig. 6. As time progresses, from left to right, the bone density increases in areas of a high mass source \mathcal{R}_0 , underneath the loading, until the density profile has converged. At biological equilibrium, right, the density ρ_0 is distributed such that the bone provides optimal structural support for forces induced during gait. The final density profile displays qualitatively similar characteristics as the subject-specific bone mineral density profile obtained from the DEXA scan shown in Fig. 1.

While a qualitative validation can be used to gain a general understanding of the density profile in response to loading, a quantitative approach is necessary for a comprehensive validation. Figure 9 shows the quantitative comparison of the region of interest method applied to both the Dual-Energy X-ray Absorptiometry scan and the two-dimensional density prediction. Squares and dotted lines indicate the experimentally measured bone mineral density extracted from the DEXA scan shown in Fig. 1. Circles and solid lines indicate the computationally predicted bone density extracted from

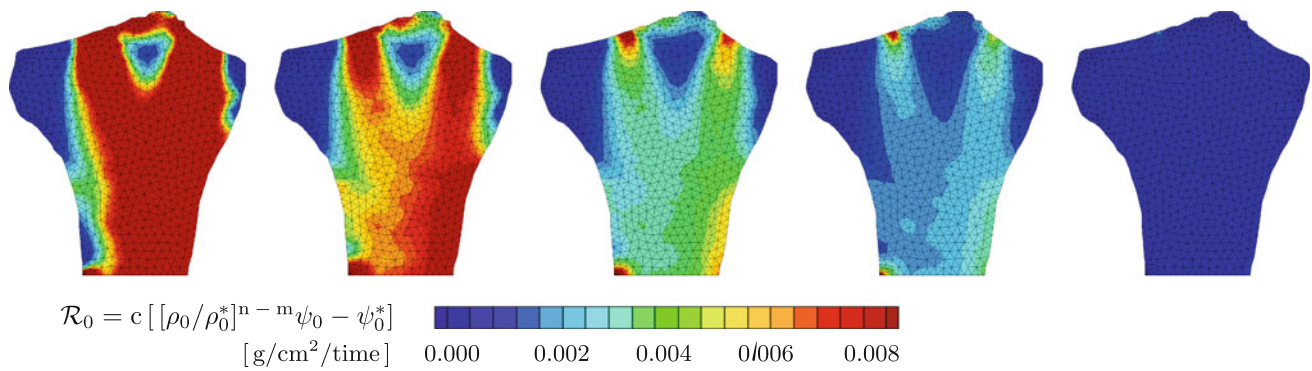


Fig. 5 Two-dimensional density prediction in the proximal tibia. The *color code* indicates the evolution of the mass source \mathcal{R}_0 , i.e., the driving force for density changes. As time progresses, from *left to right*, the bone density changes such that the strain energy

$[\rho_0/\rho_0^*]^{n-m} \psi_0$ converges toward the biological stimulus ψ_0^* . At biological equilibrium, right, both values are identical, the density source \mathcal{R}_0 vanishes, and the density ρ_0 remains unchanged

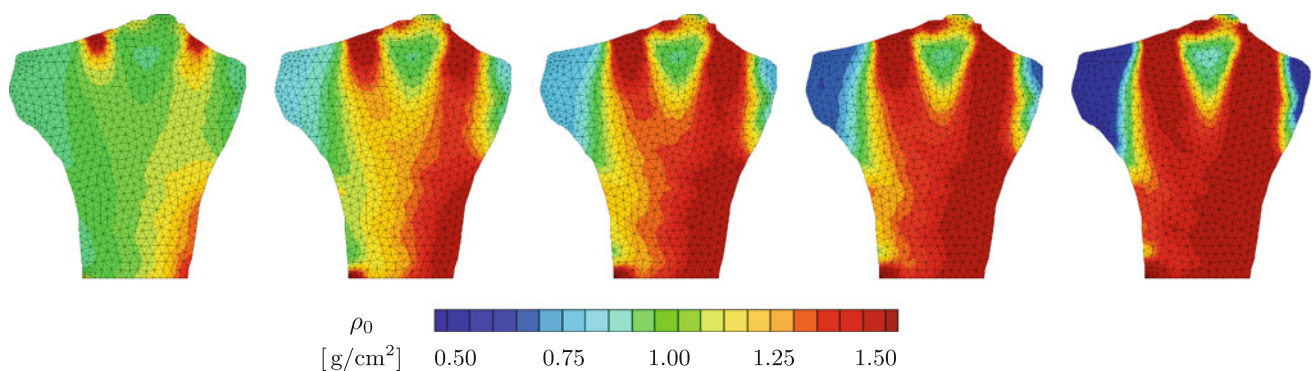


Fig. 6 Two-dimensional density prediction in the proximal tibia. The *color code* indicates the evolution of the bone density ρ_0 . As time progresses, from *left to right*, the bone density increases in areas of a high mass source \mathcal{R}_0 , underneath the loading, until the density profile has

converged. At biological equilibrium, right, the density ρ_0 is distributed such that the bone provides optimal structural support for forces induced during gait

the two-dimensional simulation shown in Fig. 6. The two-dimensional finite element model nicely captures all characteristic features of the DEXA scan. In particular, we observe two density peaks underneath the lateral and medial joint load. For the DEXA scan, the lateral density is 1.5525 g/cm² in region five, and for the simulation, it is 1.5622 g/cm². For the DEXA scan, the medial density is 1.7020 g/cm² in region twelve, and for the simulation, it is 1.7277 g/cm². The higher density in the medial region can be attributed to the loading asymmetry with 55% of the gait load applied to medial side and 45% to the lateral side, where the density is slightly lower. The region in between the loaded areas, in particular region eight, displays a characteristic low density with 1.1355 g/cm² for the DEXA scan and 1.1252 g/cm² for the simulation.

6.2 Three-dimensional density prediction

To demonstrate the feasibility of the proposed algorithm in a three-dimensional setting, we predict the bone density dis-

tribution in a three-dimensional tibia model. Figure 8 shows the resulting density profiles in the cross-sectional view, top, and in the three-dimensional view, bottom. Similar to the two-dimensional simulation, as time progresses, from left to right, the bone density ρ_0 increases in areas of high strain energy $[\rho_0/\rho_0^*]^{n-m} \psi_0$ until it converges to its equilibrium state. At biological equilibrium, right, the density ρ_0 is distributed similarly to the two-dimensional case in Fig. 6 to provide optimal structural support for forces induced during gait. From the cross-sectional view, it is obvious that our three-dimensional finite element discretization is much coarser than the two-dimensional discretization. As a result, the density profile is slightly less pronounced, but the overall trends are clearly similar.

Finally, to quantitatively compare the density profile of the three-dimensional simulation in Fig. 8 with the Dual-Energy X-ray Absorptiometry scan in Fig. 1, we extract the density distribution in the horizontal cross-section of the proximal tibia using the region of interest method. The

resulting regional variation of the bone mineral density in the fourteen regions of interest is summarized in Fig. 9. Again, the density profiles show a nice qualitative and quantitative agreement. In the loaded lateral and medial regions, regions five and twelve, the predicted bone mineral densities are 1.5593 g/cm² as compared to 1.5525 g/cm² for the DEXA scan, and 1.6907 g/cm² as compared to 1.7020 g/cm² for the DEXA scan. In the low density area of region eight, the computationally predicted bone mineral density is 1.1316 g/cm², while the experimentally measured density is 1.1355 g/cm². While all these values agree nicely, we would like to point out that the three-dimensional simulation predicts a slightly wider lower density region between the two joint loads. This discrepancy might be attributed to the fact that our three-dimensional mesh is a generic mesh that was not created based on the subject's own geometry. In addition, the mesh itself is relatively coarse in comparison to the subject-specific two-dimensional discretization. Nevertheless, we feel that even the generic three-dimensional simulation displays a good correlation with the experimentally measured density profile.

6.3 Error analysis

To quantify the error of the computational simulation with respect to the experimental measurement, we extract the bone mineral densities of the lateral and medial plateaus. Recall that these densities, BMD_{lat} and BMD_{med}, are identified as averages over three neighboring regions of interest, as indicated in Fig. 4.

Table 3 displays the absolute values of the lateral and medial bone mineral densities together with the errors of the computational prediction with respect to the experimental measurements. Errors of the subject-specific two-dimensional model are 2.73% for the lateral side and 0.99% for the medial side. Errors of the generic three-dimensional model are slightly higher with 9.33% at the lateral side and 3.99% at the medial side.

A common metric to characterize the response to loading asymmetry is the medial-to-lateral density ratio. This ratio is 1.279 for the DEXA scan, 1.327 for the two-dimensional model, and 1.122 for the three-dimensional model. Overall, the computationally predicted densities of the lateral and medial tibial plateaus are in excellent agreement with the experimental measured density values of the DEXA scan.

6.4 Potential limitations

While the density predictions in the fourteen regions of interest agree exceptionally well with our experimental measurements, the agreement in other regions is reasonable, but less strong. For example, lateral and medial to the fourteen regions, both models underestimate the local bone density

Table 3 Comparison of experimental measurement and computational predictions in terms of bone mineral densities of lateral and medial plateaus, BMD_{lat} and BMD_{med}. Errors of the computational predictions are less than 3% for the two-dimensional model, and less than 10% for the three-dimensional model. For all three approaches, the medial-to-lateral density ratio M:L ranges from 1.13 to 1.33

	DEXA [g/cm ²]	2dFEM [g/cm ²]	2derror [%]	3dFEM [g/cm ³]	3derror [%]
BMD _{lat}	1.268	1.233	2.73	1.384	9.33
BMD _{med}	1.621	1.637	0.99	1.556	3.99
	DEXA [–]	2dFEM [–]	2derror [%]	3dFEM [–]	3derror [%]
M:L-ratio	1.279	1.327	3.83	1.122	12.18

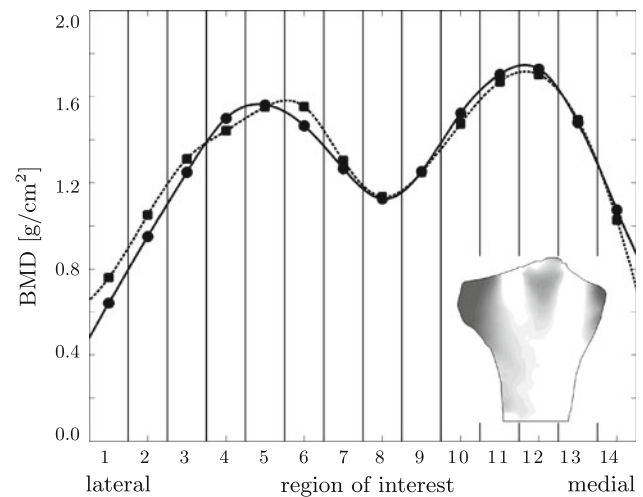


Fig. 7 Regional variation of bone mineral density in fourteen regions of interest. Squares and dotted lines indicate the experimentally measured bone mineral density extracted from the Dual-Energy X-ray Absorptiometry scan shown in Fig. 1. Circles and solid lines indicate the computationally predicted bone density extracted from the two-dimensional simulation shown in Fig. 6

with values of 0.5 g/cm² or less, indicated through the dark blue colors in Figs. 6, 7, 8, and 9. We suggest that these discrepancies can be explained by the following limitations of the model.

Firstly, we have assumed that the bone possesses similar material properties in every element. In reality, the collagen matrix in the subchondral bone is far from uniform in terms of its material properties. For more detailed studies, we recommend to use a finer mesh in which the outer layer is modeled as cortical bone, while all internal elements are modeled as trabecular bone. Ideally, the cortical bone layer would then have a higher initial density compared to its internal counterpart and its density would not be allowed to change over time.

Secondly, we have simplified the tibiofemoral loading through two representative forces acting on a single medial

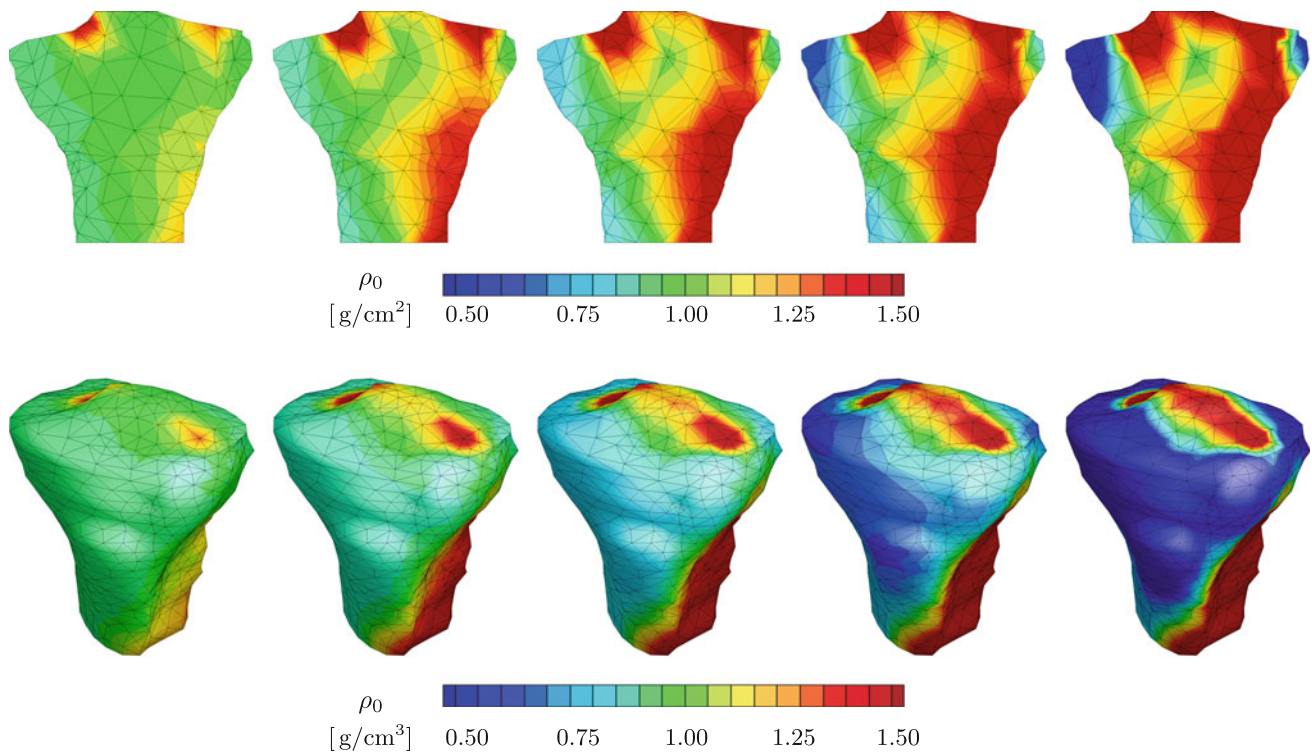


Fig. 8 Three-dimensional density prediction in the proximal tibia. The color code indicates the evolution of the bone density ρ_0 . As time progresses, from left to right, the bone density increases in areas of high strain energy $[\rho_0/\rho_0^*]^{n-m} \psi_0$ until it has converged. At bio-

logical equilibrium, right, the density ρ_0 is distributed such that the bone provides optimal structural support for forces induced during gait. Density evolution is displayed in the cross-sectional view, top, and in the three-dimensional view, bottom

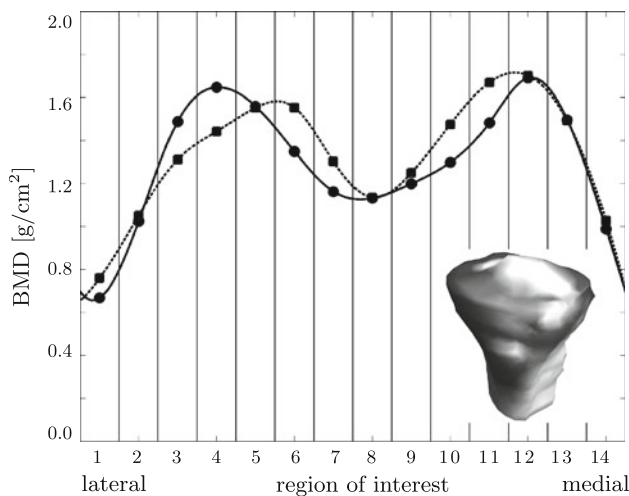


Fig. 9 Regional variation of bone mineral density in fourteen regions of interest. Squares and dotted lines indicate the experimentally measured bone mineral density extracted from the Dual-Energy X-ray Absorptiometry scan shown in Fig. 1. Circles and solid lines indicate the computationally predicted bone density extracted from the cross-sectional view of the three-dimensional simulation shown in Fig. 8, top

and lateral node each. However, in reality, the articular cartilage interface between the femur and tibia can be strained, the

loading can shift in location, and, most importantly, spread over an entire area. We recommend further investigations to precisely specify the relevant types of loading and points of action.

Thirdly, we have neglected forces from muscles, tendons, and the tibiofemoral joint. During the swing and stance phases, the hamstrings and the quadriceps femoris flex, and exert contractile forces on the tibiofemoral joint, which indirectly add loading to the subchondral bone. Integrating the force contributions from the surrounding tissues would likely improve the validity of the model. Lastly, for the finite element boundary conditions, we have assumed that the subchondral bone was in complete isolation. A more accurate model would include a finite contact region with the proximal fibula and ideally mimic the in vivo loading situation through an elastic foundation.

In addition to these technical limitations, our current model only accounts for mechanical factors as driving forces for density adaptation, entirely neglecting biochemical factors, age, gender, race, or family history. From a clinical point of view, density adaptation and bone fracture are multifactorial processes, which cannot be characterized by bone mineral density alone. We would like to reiterate though, that at this stage, our model is not meant to be a diagnostic tool

for osteoporosis or fracture risk, but rather a research tool to provide insight into changes in density profiles in response to mechanical loading.

Overall, the present model shows promise in predicting medial and lateral densities, but offers room for further improvement. Crucial input parameters such as the initial density, the amount of loading, and the loading locations are constructed to be controllable. Therefore, the model can be easily extended to predict bone mineral densities in subjects with different loading conditions such as obese individuals or high powered athletes.

7 Discussion

The goal of this manuscript was to explore the potential of two- and three-dimensional finite element models to predict the bone density distribution in the proximal tibia in response to gait-induced loading. This work was motivated by the hypothesis that cyclic dynamic loading during gait does significantly impact the subchondral bone density. This phenomenon has been thoroughly investigated in the past through various clinical trials, mainly focussing on the effects of osteoarthritis. However, none of these trials has used finite element models as predictors. In a comprehensive bone density analysis, we have initiated a multi-faceted series of studies including gait analysis, Dual-Energy X-ray Absorptiometry, bone mineral density analysis, and two- and three-dimensional finite element analyses to integrate data from multiple sources.

Using the theory of open system thermodynamics, we have designed a stable and robust finite element framework in which heterogeneous density profiles in hard biological tissues evolve naturally in response to mechanical over or underload. To characterize the critical forces in the tibiofemoral joint, we have performed a subject-specific gait analysis using an inverse dynamics approach. We have imported the resulting medial and lateral forces during the midstance phase of gait into a fully nonlinear finite element-based density analysis.

To validate our computational model, we have taken a Dual-Energy X-ray Absorptiometry scan, from which we have directly created a two-dimensional subject-specific geometric model of the proximal tibia. For the three-dimensional simulation, we have generated a generic geometric model from a magnetic resonance image of a randomly selected adult right knee from our data base. We have demonstrated an excellent qualitative agreement of the computationally predicted density profiles with the experimentally measured bone mineral density distribution. To demonstrate the quantitative agreement of the predicted and measured density profiles, we have adopted the region of interest method and

extracted discrete density values using standard and custom-designed image analysis tools.

Overall, the computationally predicted density profiles have displayed errors of less than 3% for the two-dimensional simulation and of less than 10% for the three-dimensional simulation. In summary, we believe that the proposed computational method has a tremendous potential to identify changes in bone mineral density in response to altered mechanical loading. As such, our framework has the potential to accurately address the complex interactions between ambulatory loads and tissue changes, and improve the long-term success of possible treatment options for chronic diseases such as osteoarthritis on a patient-specific basis.

Acknowledgments This work is the result of a final project for the Stanford graduate class ME337 Mechanics of Growth. The authors would like to acknowledge the support of Katerina Blazek, Phil Cutti, Nathan Netravali, Saikat Pal, Jonathan Rylander, the Biomotion Laboratory, and the Human Performance Laboratory at Stanford University. This material is based on work supported by the National Science Foundation CAREER award CMMI-0952021 and by the National Institutes of Health Grant U54 GM072970.

References

- Altman RD (2010) New guidelines for topical NSAIDs in the osteoarthritis treatment paradigm. *Curr Med Res Opin* 26:2871–2876
- Ambrosi D, Ateshian GA, Arruda EM, Cowin SC, Dumais J, Goriely A, Holzapfel GA, Humphrey JD, Kemkemmer R, Kuhl E, Olberding JE, Taber LA, Garikipati K (2011) Perspectives on biological growth and remodeling. *J Mech Phys Solids* 59:863–883
- Andriacchi TP (1994) Dynamics of knee malalignment. *Orthop Clin North Am* 25:395–403
- Andriacchi TP, Natarajan RN, Hurwitz DE (1997) Musculoskeletal dynamics, locomotion, and clinical applications. In: Mow VC, Hayes WC (eds) *Basic orthopaedic biomechanics*. 4th edn. Lippincott-Raven, Philadelphia pp 37–67
- Andriacchi TP, Mündermann A, Smith RL, Alexander EJ, Dyrby CO, Koo S (2004) A framework for the in vivo pathomechanics of osteoarthritis at the knee. *Ann Biomed Eng* 32:447–457
- Baliunas AJ, Hurwitz DE, Ryals AB, Karrar A, Case JP, Block JA, Andriacchi TP (2002) Increased knee joint loads during walking are present in subjects with knee osteoarthritis. *Osteoarthr Cartil* 10:573–579
- Bolotin HH (2007) DXA in vivo BMD methodology: an erroneous and misleading research and clinical gauge of bone mineral status, bone fragility, and bone remodelling. *Bone* 41:138–154
- Bone HG, Santora AC, Chattopadhyay A, Liberman U (2005) Are we treating women with postmenopausal osteoporosis for their low BMD or high fracture risk? *J Bone Min Res* 20:2064–2065
- Carpenter RD, Carter DR (2010a) The mechanobiological effects of periosteal surface loads. *Biomech Model Mechanobiol* 7:227–242
- Carpenter RD, Carter DR (2010b) Computational simulation of spontaneous bone straightening in growing children. *Biomech Model Mechanobiol* 9:317–328
- Carter DR, Hayes WC (1977) Compressive behavior of bone as a 2-phase porous structure. *J Bone Joint Surg* 59:954–962
- Cowin SC, Hegedus DH (1976) Bone remodelling I: theory of adaptive elasticity. *J Elast* 6:313–326

- Dequeker J, Mokassa L, Aerssens J, Boonen S (1997) Bone density and local growth factors in generalized osteoarthritis. *Microsc Res Tech* 37:358–371
- Gandolini G, Salvioni PM (2004) Is BMD measurement an adequate surrogate for anti-fracture and efficacy? *Aging Clin Exp Res* 16:29–32
- Gitman I, Askes H, Kuhl E, Aifantis EC (2010) Stress concentrations in fractured compact bone simulated with a special class of anisotropic gradient elasticity. *Int J Solids Struct* 47:1099–1107
- Hambli R, Katerchi H, Benhamou CL (2011) Multiscale methodology for bone remodelling simulation using coupled finite element and neural network computation. *Biomech Model Mechanobiol* 10:133–145
- Harrigan TP, Hamilton JJ (1993) Finite element simulation of adaptive bone remodelling: a stability criterion and a time stepping method. *Int J Numer Methods Eng* 36:837–854
- Himpel G, Kuhl E, Menzel A, Steinmann P (2005) Computational modelling of isotropic multiplicative growth. *Comput Methods Eng Sci* 8:119–134
- Huiskes R, Weinans H, Grootenboer HJ, Dalstra M, Fudala B, Slooff TJ (1987) Adaptive boneremodeling theory applied to prostheticdesign analysis. *J Biomech* 20:1135–1150
- Hulet C, Sabatier JP, Souquet D, Locker B, Marcelli C, Vielpeau C (2002) Distribution of bone mineral density at the proximal tibia in knee osteoarthritis. *Calcif Tissue Int* 71:315–322
- Hunter DJ, Felson DT (2006) Osteoarthritis. *Br Med J* 332:639–642
- Hurwitz DE, Summer DR, Andriacchi TP, Sugar DA (1998) Dynamic knee loads during gait predict proximal tibial bone distribution. *J Biomech* 31:423–430
- Jacobs CR, Levenston ME, Beaupre GS, Simo JC, Carter DR (1995) Numerical instabilities in bone remodeling simulations: the advantages of a node-based finite element approach. *J Biomech* 28:449–459
- Kaptoge S, Benevolenskaya LI, Bhalla AK, Cannata JB, Boonen S, Falch JA, Felsenberg D, Finn JD, Nuti R, Hoszowski K, Lorenc R, Miazgowski T, Jajic I, Lyrilis G, Masaryk P, Naves-Diaz M, Poor G, Reid DM, Scheidt-Nave C, Stepan JJ, Todd CJ, Weber K, Woolf AD, Roy DK, Lunt M, Pye SR, O'Neill TW, Silman AJ, Reeve J (2005) Low BMD is less predictive than reported falls for future limb fractures in women across Europe: results from the European prospective osteoporosis study. *Bone* 36:387–398
- Kuhl E, Menzel A, Steinmann P (2003) Computational modeling of growth—a critical review, a classification of concepts and two new consistent approaches. *Comput Mech* 32:71–88
- Kuhl E, Steinmann P (2003a) Theory and numerics of geometrically nonlinear open systems. *Int J Numer Methods Eng* 58: 1593–1615
- Kuhl E, Steinmann P (2003b) Mass- and volume specific views on thermodynamics for open systems. *Proc Royal Soc Lond* 459:2547–2568
- Kuhl E, Steinmann P (2003c) On spatial and material settings of thermo-hyperelastodynamics for open systems. *Acta Mech* 160:179–217
- Kuhl E, Steinmann P (2004) Material forces in open system mechanics. *Comput Methods Appl Mech Eng* 193:2357–2381
- Lancianese SL, Kwok E, Beck CA, Lerner A (2008) Predicting regional variations in trabecular bone mechanical properties within the human proximal tibia using MR imaging. *Bone* 43:1039–1046
- Menzel A (2005) Modelling of anisotropic growth in biological tissues—a new approach and computational aspects. *Biomech Model Mechanobiol* 3:147–171
- Morrison JB (1970) The mechanics of the knee joint in relation to normal walking. *J Biomech* 3:51–61
- Nielsen SP (2000) The fallacy of BMD: a critical review of the diagnostic use of dual X-ray absorptiometry. *Clin Rheumatol* 19:174–183
- Radin EL, Rose RM (1986) Role of subchondral bone in the initiation and progression of cartilage damage. *Clin Orthop Relat Res* 213:34–40
- Reina-Romo E, Gomez-Benito MJ, Garcia-Aznar JM, Dominguez J, Doblare M (2010) Growth mixture model of distraction osteogenesis—effect of pre-traction stresses. *Biomech Model Mechanobiol* 9:103–115
- Schipplein OD, Andriacchi TP (1991) Interaction between active and passive knee stabilizers. *J Orthop Res* 9:113–119
- Taylor RE, Zheng C, Jackson RP, Doll JC, Chen JC, Holzbaur KRS, Besier T, Kuhl E (2008) The phenomenon of twisted growth: humeral torsion in dominant arms of high performance tennis players. *Comput Methods Biomech Biomed Eng* 12:83–93
- Weinans H, Huiskes R, Grootenboer HJ (1992) The behavior of adaptive bone-remodeling simulation models. *J Biomech* 25:1425–1441
- Zhang J, Michalenko MM, Kuhl E, Ovaert TC (2010) Characterization of indentation response and stiffness reduction in bone using a continuum damage model. *J Mech Behav Biomed Mater* 3:189–202
- Zhao D, Banks SA, D'Lima DD, Colwell CW, Fregly BJ (2007) In vivo medial and lateral tibial loads during dynamic and high flexion activities. *J Orthop Res* 25:593–602